JOURNAL OF PHYSIOLOGY AND PHARMACOLOGY 2009, 60, Suppl 4, 83-93
www.jpp.krakow.pl

L.W. DOBRUCKI[1], B.J. MARSH[2,3,4,5], L. KALINOWSKI[6]

ELUCIDATING STRUCTURE-FUNCTION RELATIONSHIPS FROM MOLECULE-TO-CELL-TO-TISSUE: FROM RESEARCH MODALITIES TO CLINICAL REALITIES

[1]Section of Cardiovascular Medicine, Department of Internal Medicine, Yale University School of Medicine, New Haven, Connecticut, U.S.A.; [2]Institute for Molecular Bioscience, [3]Centre for Microscopy and Microanalysis, [4]ARC Centre of Excellence in Bioinformatics St Lucia, Australia; [5]School of Chemistry and Molecular Biosciences, The University of Queensland, St Lucia, Australia; [6]Department of Medical Laboratory Diagnostics, Chair of Clinical Chemistry and Biochemistry, Medical University of Gdansk, Gdansk, Poland

The National Academy of Engineering selected 'Imaging' as one of the greatest engineering achievements of the 20th century (Greatest Engineering Achievements of the 20th Century. 2009 (cited 2008, November 10); available from: http://www.greatachievements.org/). The combination of different imaging modalities and technologies for mapping bimolecular and/or biological processes within single cells or even whole organs has extraordinary potential for revolutionizing the diagnosis and treatment of pathophysiological disorders, and thus for mitigating the significant social and economic costs associated with the clinical management of disease. Such integrated imaging approaches will eventually lead to individualized programs for disease prevention through advanced diagnosis, risk stratification and targeted cell therapies resulting in more successful and efficient health care. The goal of this article is to provide readers with a current update of selected of state-of-the-art imaging modalities which would likely to lead to improved clinical outcomes if employed in an integrated approach, including use of ultramicrosensors to detect reactive oxygen/nitrogen species in a single cell, use of electron tomography to visualize and characterize cellular organization in three dimensions (3D), and molecular imaging strategies to assess naturally occurring and therapeutic peripheral and myocardial angiogenesis using targeted radiolabeled tracers.

Key words: *biosensors, nitric oxide, superoxide, peroxynitrite, endothelium, endothelial nitric oxide synthase, cellular tomography, electron microscope tomography, 3D reconstruction, mammalian, insulin, secretion, beta cell, islets of Langerhans, angiogenesis, imaging of angiogenesis, integrins, single photon emission computed tomography, positron emission tomography*

VASOPROTECTION BY NO: eNOS AS A NOVEL THERAPEUTIC TARGET

Over the last two decades, it has become evident that the endothelium is not merely an inert, single-cell lining that covers the internal surface of blood vessels, but in fact plays a crucial role in regulating vascular function. Although serving as an extremely active endocrine and paracrine organ that produces a large variety of molecules participating in complex biochemical processes, the simple product generated by endothelial nitric oxide synthase (eNOS) - nitric oxide (NO) - seems to be the key molecule required for the maintenance of vascular homeostasis (1-4). For example, NO produced by eNOS causes vasodilation. Thus, eNOS knockout mice are hypertensive (5), whereas eNOS transgenic mice exhibit hypotension (6). In addition, NO reduces the activation and aggregation of platelets, attenuates adhesion of leukocytes to the endothelium, reduces the permeability of the endothelium, and inhibits proliferation and migration of vascular smooth muscle cells. Impaired activity of eNOS and the loss of NO bioavailability are associated with endothelial cell dysfunction that is itself an independent risk factor for cardiovascular diseases (2, 3). Several factors contribute to loss of NO bioavailability, including reduced NO synthesis and NO scavenging O_2^-. Under physiological conditions, there is a balance between endothelial NO and O_2^- production. However, vascular diseases are associated with increased O_2^- generation, and several oxidase systems contribute to increased oxidative stress, notably NADPH-dependent oxidases and eNOS itself (1). Under oxidant stress, production of O_2^- and its derived oxidants, including peroxynitrite ($ONOO^-$), induce eNOS dysfunction with uncoupling of the enzyme leading to the production of NOS-derived O_2^- instead of NO. It has been shown that an imbalance between NO and O_2^- can contribute to the onset of a variety of cardiovascular disease states such as atherosclerosis, thrombosis, hypertension, diabetes mellitus, heart failure, post-angioplasty restenosis, cerebral vasospasm and delayed wound healing (2, 3). Therefore, tight coupling of the enzyme is important for normal cardiovascular function and thus prevention of disease onset.

Regulation of eNOS coupling

The catalytic domains of NOS include a flavin-containing NADPH binding reductase and a heme-binding oxygenase, that also contains the binding site labile cofactor tetrahydrobiopterin

(BH_4) and the substrate L-arginine (1, 7). In the presence of Ca^{2+} and calmodulin, electrons flow from NADPH through the reductase domain to the oxygenase domain resulting in the activation of oxygen at the heme center followed by the substrate monooxygenation. This process requires the presence of the fully reduced BH_4 and appropriate L-arginine availability. One of the primary mechanisms implicated in the oxidant-induced switch of eNOS from the production of NO to the generation of O_2^- is the oxidation of the enzyme-bound BH_4 and/or disruption of the zinc-thiolate complex.

Various extracellular signals, including shear stress and additional stimuli such acetylcholine, bradykinin, vascular endothelial growth factor (VEGF), estrogen, sphingosine 1-phosphate and aldosterone, modulate eNOS-derived NO generation through several transduction pathways. Cellular studies have demonstrated that phosphorylation of eNOS at specific amino acids regulates enzyme-mediated NO production (8). With this line, it has been reported that protein kinase B (Akt) specifically induces phosphorylation of Ser-1177 and protein kinase C specifically phosphorylates Thr-495. Although phosphorylation of Ser-1177 has been shown to increase NO production from eNOS (9), in contrast, phosphorylation of Thr-495, has been demonstrated to down-regulate NO generation (10, 11). Furthermore, other studies have revealed that phosphorylation can regulate O_2^- in addition to NO generation from eNOS (12). It has been shown that phosphorylation of Ser-1177 greatly increases O_2^- generation, by altering both the Ca^{2+} sensitivity of the enzyme and the rate of product formation, toward eNOS-dependent O_2^- generation becoming largely Ca^{2+}-independent. Thr-495 phosphorylation, in turn, indirectly regulates eNOS function through regulation of the calmodulin and caveolin interaction, but this is not necessarily associated with a decrease in eNOS-dependent O_2^- formation.

It should be noted that O_2^- reacts rapidly with NO to form $ONOO^-$, which is a strong biological oxidant known to oxidize lipids, proteins, sylfhydryls, and DNA and to cause nitration of tyrosines (13). On the one hand, it has been suggested that $ONOO^-$ uncouples eNOS by oxidation of the zinc-thiolate complex that comprises the BH_4 binding site; this in turn leads to dissociation of eNOS dimers to monomers (14). On the other hand, it has been suggested that BH_4 *per se* is an important target for oxidation by $ONOO^-$ (15, 16). Of note, $ONOO^-$ is more potent than either O_2^- or H_2O_2 in causing oxidation of BH_4 (15, 17, 18). It has been shown that treatment of purified eNOS with $ONOO^-$ significantly decreased the ability of the enzyme to produce NO. Furthermore, $ONOO^-$ strikingly increased vascular O_2^- production in vessels from control mice but not in vessels from eNOS-deficient mice, suggesting that eNOS was the source of O_2^- (17). Thus, it is possible that both the zinc-thiolate center and BH_4 are targets of oxidation by $ONOO^-$, particularly when high levels of this oxidant are present.

Evaluation of eNOS activity: biosensors for concurrent detection of NO, O_2^- and $ONOO^-$

Given the beneficial effects of endothelial NO, an increase of eNOS activity by pharmacological means or (local) gene therapy, could be possibly beneficial in patients at increased risk of cardiovascular diseases. However, eNOS-derived NO also has detrimental effects, such as the generation of O_2^-, making it difficult to predict whether increased eNOS activity is beneficial of harmful. To determine whether increased eNOS activity may be beneficial, we have generated ultramicrosensors for NO, O_2^- and $ONOO^-$, combined into one working unit, which allow us to measure concurrently NO, O_2^- and $ONOO^-$ concentrations in real time in a single cell (*Fig. 1*). Each microsensor was made by electroplating a sensing material, a specific polymeric complexes with metalloporphyrin or enzyme, on the tip of carbon fiber (length 1 mm, diameter 0.5 μm) to facilitate the electron transfer on or from the detected molecule to the sensor (*Fig. 2*). The fibers were sealed with nonconductive epoxy and electrically connected to copper wires with conductive silver epoxy. The following conductive polymeric films were applied: nickel(II)tetrakis (3-methoxy-4-hydroxyphenyl) porphyrin for the sensor of NO, an immobilized polypyrrole/horseradish peroxidase (PPy/HRP) for the sensor of O_2^- and manganese(III)-[2,2]paracyclophany-lporphyrin for the sensor of $ONOO^-$. In addition, the sensors for NO and $ONOO^-$ were supercoated with a negatively charged polymer (nafion) for NO sensor or positively charged dopamine for $ONOO^-$ sensor that repelled or retarded charged species while allowing NO or $ONOO^-$ access to the underlying catalytic surface. A three-electrode system, which includes the tandem NO, O_2^-, ONOO -sensors as a working electrode, counter platinum electrode, and calomel reference electrode, was used with constant potentials of 0.65 V for NO detection, -0.45 V for $ONOO^-$ detection and -0.23 V for O_2^- detection. The system was coupled with potentiostat (*e.g.* Gamry Reference 600 multichannel) and personal computer with electrochemical software (*e.g.* VFP600, Gamry Instruments, Warminster, PA, USA). The tandem sensors are highly sensitive for NO, O_2^-, $ONOO^-$ (10^{-9} mol/L detection limit for each sensor), and their response time is rapid (on the order of 10^{-4} s each), providing the ability to make kinetic

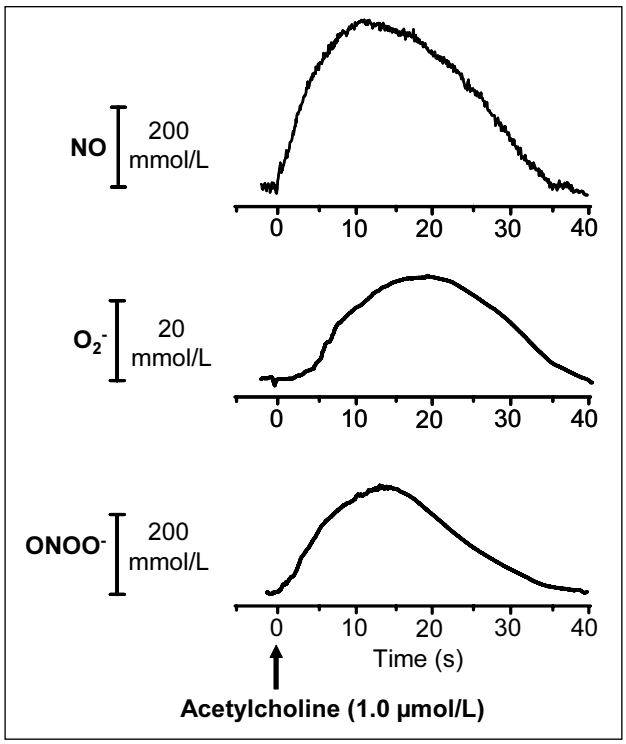

Fig. 1. Typical amperogram curves showing kinetics of nitric oxide (NO) (A), superoxide (O_2^-) (B), and peroxynitrite ($ONOO^-$) (C) release from a single endothelial cell after endothelial nitric oxide synthase (eNOS) stimulation. eNOS was stimulated with 1 μmol/L calcium ionophore (CaI; A23187). The experiments were made on the endothelium obtained from aortic rings isolated from normal rats. While considering the effect of potent eNOS agonists, it should be born in mind that activation of NO release by any eNOS agonists species in endothelial cells is always associated with increase release of both O_2^- and $ONOO^-$. Therefore, measurement of NO/O_2^-/$ONOO^-$ ratio in the timecourse of action of a vasoactive agent is an especially valuable approach for estimation of its therapeutic benefits.

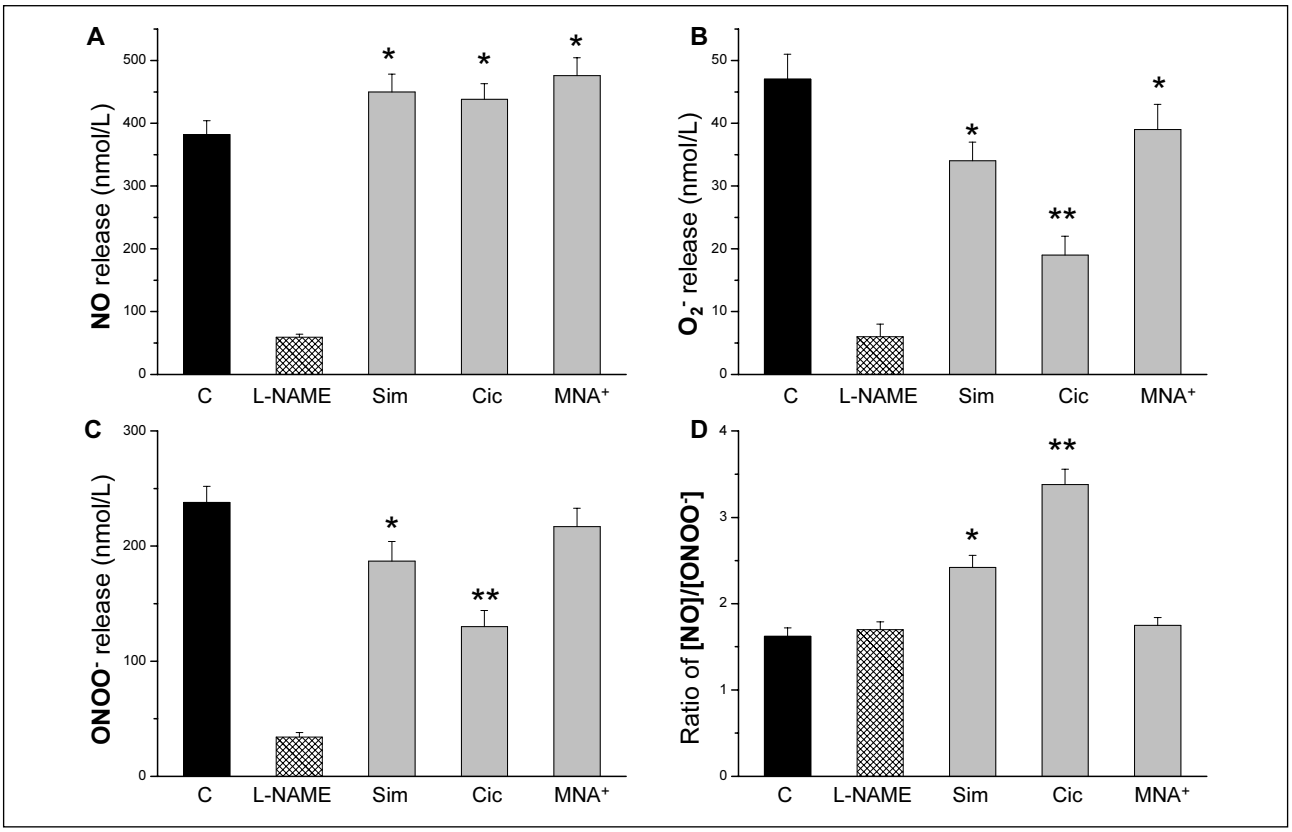

Fig. 2. A maximal nitric oxide (NO) (*A*), superoxide (O_2^-) (*B*), and peroxynitrite ($ONOO^-$) (*C*) concentrations produced by the endothelial cells (rat aorta) in the presence of 300 μmol/L N^G-nitro-L-arginine methyl ester (L-NAME), 1 μmol/L simvastatin (Sim), 1 μmol/L cicletanine (Cic; (±)3-(4chlorophenyl)-1,3-dihydro-7-hydroxy-6-methylfuro-[3,4-c] pyridine) 3-(4-chlorophenyl)-1,3-dihydro-7-hydroxy-6-methylfuro-[3,4-c] pyridine) or 1 μmol/L 1-methylnicotinamide (MNA^+). The ratio of NO concentration to the $ONOO^-$ concentration represents the index of nitroxidative stress (*D*); higher [NO/$ONOO^-$] indicates stronger eNOS coupling and greater bioavailability of NO within the cells. The aortic rings isolated from normal rats were incubated in the incubation chamber for 30 minutes with the tested substance prior to CaI addition. Inhibition of NO production by L-NAME with concurrent inhibition of O_2^- and $ONOO^-$ formation during activation of eNOS supports the concept that uncoupling of eNOS occurs in intact endothelial cells. Among the tested substances, the action of cicletanine followed by simvastatin and 1-methylnicotinamide demonstrates the most favorable potency toward the restoration of the disturbed eNOS-dependent NO/O_2^-/$ONOO^-$ balance after maximal stimulation of the enzyme by CaI. **P*<0.01 and ***P*<0.001 vs. CaI alone (C), n = 5-6 experiments. The data are presented as means ±SE. Multiple comparisons were evaluated using ANOVA followed by the Student's test.

measurements of the detected molecules concentrations. The active tips of the sensors system were maintained close to the surface of a single endothelial cell with help of computer-controlled micromanipulator.

Until the electrochemical concurrent measurements of NO, O_2^-, $ONOO^-$ were applied *in situ* by using the ultramicrosensors, it was totally unclear whether O_2^- production by dysfunctional eNOS occurs only under specific pathological conditions or whether it also occurs to some extent in normal endothelium that is not exposed to cardiovascular risk factors. We have shown for the first time that these mechanisms tightly regulate the delicate balance between NO, O_2^- and $ONOO^-$ at different redox levels within native endothelial cells, and may thus help to explain why some individuals seem predisposed to endothelial vasodilator dysfunction (19). Application of these sensors in our studies enabled us to demonstrate that the steady state of NO, O_2^- and $ONOO^-$ balance within endothelial cells can be modified by pharmacological intervention (19-26). We provided direct evidence that some drugs are potent in terms of their capacity to increase NO bioavailability in endothelial cells through preservation of eNOS function, and may have clinical application for either the prevention of endothelial dysfunction (by preservation of eNOS coupling) or the restoration of endothelial dysfunction (by reversal of eNOS uncoupling). These novel pharmacological properties associated with an increase of NO bioavailability are revealed by the well-known drugs (such as HMG-CoA reductase inhibitors and furopirydine derivative cicletanine) as well as an endogenous compound, 1-methylnicotinamide, a primary metabolite of nicotinamide, that until recently was thought to be biologically inactive (*Fig. 3*).

In conclusion, although eNOS has been suggested as a potential target for treatment in human endothelium, upregulation of eNOS function might not always be good. eNOS uncoupling seems to be present in numerous common diseases, as well as in native endothelial cells of healthy humans. This is an important caveat for clinical strategies aimed at pharmacological intervention to target eNOS activity or eNOS expression, since enzyme upregulation might even aggravate vascular damage in such cases. The net effect of the reaction between NO and O_2^- compromises reduction of concentration of both products as well as the biological effects of $ONOO^-$ itself. Thus, increased production of a deleterious metabolite, $ONOO^-$, by eNOS, may shift the balance between oxidative and reductive states of the endothelial cell (towards nitroxidative stress) and may alter the beneficial effects of increased NO activity. Detection of NO together with concurrent detection of O_2^- and $ONOO^-$, localized to

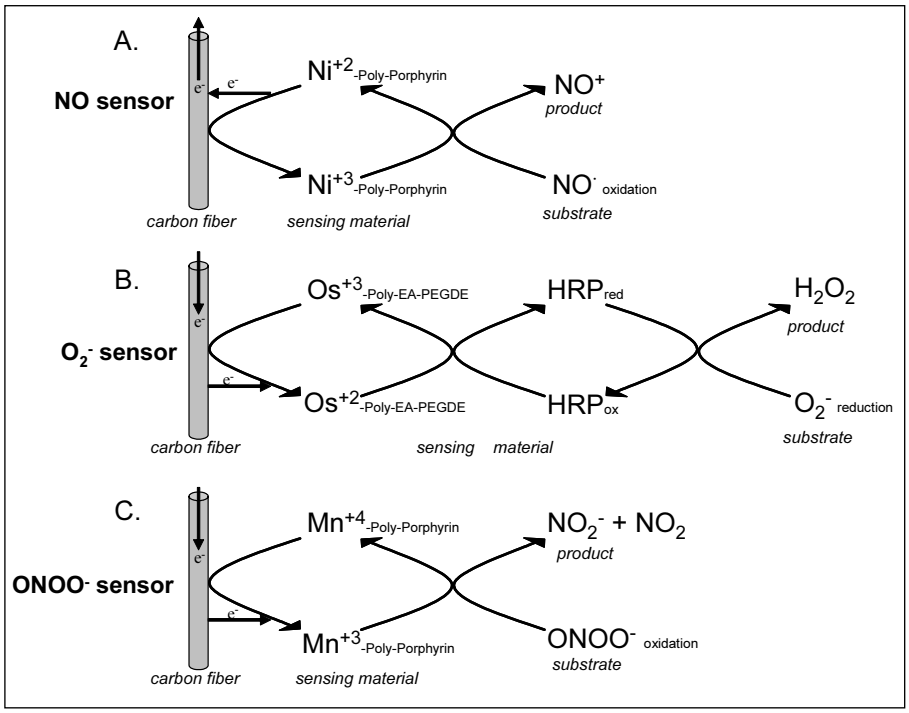

Fig 3. A cyclic reaction mechanism during the signal transduction (from chemical into electrical) by the sensing material (the complexes of organic polymers with metal ions) of nitric oxide (NO) sensor (*A*), superoxide (O_2^-) sensor (*B*) and peroxynitrite ($ONOO^-$) sensor (*C*). HRPred, HRPox – reduced and oxidized forms of horseradish peroxidase, respectively; Ni^{+2}/Ni^{+3}-Poly-Porphyrin – poly-nickel(II/III) tetrakis(3-methoxy-4-hydroxyphenyl) porphyrin; Os^{+2}/Os^{+3}-Poly-EA-PEGDE-HRP – complexes of cis-[osmium(II/III)$(bpy)_2$ Cl_2]-[poly(4-vinyl-pyridine)] and poly (ethylene glycol)diglycidyl ether and horseradish peroxidase; Mn^{+3}/Mn^{+4}-Poly-Porphyrin – poly-manganese(III/IV)-[2,2]paracyclophanylporphyrin.

the vicinity of eNOS in operation (surface of the cell membrane), offers the advantage of for precisely evaluating the extent of eNOS uncoupling, since the measurements are made *in situ* in real time, and in the location with the highest concentrations of the detected molecules. Consequently, this approach affords the most efficient and accurate means for testing compounds that may potentially have beneficial effects by targeting the endothelium for improved eNOS function and nitroxidative stress.

3D ELECTRON MICROSCOPY OF MAMMALIAN CELLS AND TISSUES

Since the first images of cultured mammalian cells taken on an electron microscope (EM) by Albert Claude, Ernest Fullam and Keith Porter were published in the United States in 1945 (27), the ultrastructural analysis of mammalian cells and tissue has relied almost entirely on the interpretation of two-dimensional (2D) images to deduce the three-dimensionality of the organelles, cells and/or tissue under study. However, over the past decade, electron microscope tomography (ET) - also often referred to as 'electron tomography' or 'cellular tomography' - has emerged as a powerful research tool for studying mammalian cell and tissue biology in 3D *in situ*, in an appropriate physiological context (28-33). ET uses mathematical techniques to computationally reconstruct a 3D volume from a set of accurately aligned 2D images, in a manner similar to clinical/diagnostic 3D imaging techniques such as computed tomography (CT), magnetic resonance imaging (MRI) and positron emission tomography (PET), as discussed in more detail elsewhere in this article (34). However, rather than computing a 3D reconstruction of a patient's (or an animal's) anatomy, a 3D snapshot revealing a cell's anatomy is produced, but at approximately 10^5-10^6 times higher resolution (*i.e.* ~5 nm) than for our clinical imaging counterparts listed above (35-37).

Methods

Ideally, high resolution cellular imaging studies by ET are undertaken on tissue prepared using advanced cryo-preparation techniques so that the physiological state and architecture of the cell(s) of interest is captured as reliably as possible (38-41), with the obvious exception of cases where the physiology and/or physical location of the tissue under study makes this impractical (42). By stopping all cellular processes in a matter of milliseconds using a 'fast-freezing' approach, delicate structures and dynamic events are immobilized in a 'close-to-native' state (43, 44). Typically, such 'frozen-hydrated' cells are then processed for EM at ultra-low temperatures using a method called 'freeze-substitution', and are subsequently infiltrated with resin. After plastic-embedding, the tissue is sliced into sequential slabs called 'sections', each about 250-400 nm thick, which can be viewed and imaged either individually or in series (38, 39). Thick sections are cut rather than conventional thin (60-100 nm) sections in order to visualize as much of the depth of the specimen as quickly as possible as well as minimize disruption of the tissue by reducing the number of times the specimen has to be physically cut or 'sectioned'. It is worth noting that many dozens of such serial 'thick' sections are needed to span the entire volume of a single mammalian cell (45). 2D images are then collected in an EM that operates at higher-than-normal voltages (*e.g.* ≥300 keV compared to conventional EMs that operate in the range of 80-120 keV), as the section is serially tilted by small, regular increments (*e.g.* 1° or 1.5°) over a relatively large angular tilt range (*e.g.* ±60-70°). These sets of images – referred to as a 'tilt series' - are initially aligned with one another using a mathematical technique called 'cross-correlation', which uses information common within each image to bring the tilt series images crudely into register. The images are then aligned more accurately by precisely tracking the positions of small gold fiducial markers placed on the top and bottom of each section prior to imaging in the EM, and a 3D density distribution or 'tomogram' is computed from each set of aligned tilts around a single-axis using another mathematical technique referred to as 'weighted back-projection' (30). However, for cellular tomography, tilt series data are preferentially collected around two orthogonal axes rather than just a single axis because the resolution of an object within the plane of a specimen that has a slab geometry - such as a thick slice (*i.e.* 'section') cut from plastic-embedded cells and/or tissue - also depends on its

orientation relative to the axis around which the specimen is tilted. In this case, individual tomograms generated for each axis are brought into register and then combined in 3D to produce a dual-axis reconstruction that exhibits improved symmetry and resolution in all three dimensions.

However, due to the scale and complexity of the image data that are represented in 3D reconstructions of cellular volumes generated using this approach, detailed image segmentation/analysis is necessary before meaningful biological insights can be made. However, once segmented and meshed, not only can organelles and other structures (*e.g.* ribosomes and microtubules) be viewed unambiguously in 3D either alone or in context with any other object(s) or combination of object(s), but precise quantitative measurements (*e.g.* membrane surface area and volume) can be obtained relatively quickly using the triangular mesh information for each object. Unfortunately, however, due to the relatively low signal-to-noise ratio (from a mathematical perspective) that is characteristic for these kinds of EM data, most automated/algorithmic segmentation approaches have to date yielded poor results. Instead, cellular tomograms must be painstakingly segmented by manually outlining the membrane boundaries of objects of interest on each pixel-thick tomographic slice using drawing tools available in software analysis packages specialized for complex 3D biological image data such as *IMOD* (46), in order to build up a 'contour map' in the Z dimension from which a 3D surface can be generated for subsequent visualization and morphometric analysis. Consequently, image segmentation represents the major 'rate-limiting step' for ongoing discovery through a 3D 'cell mapping' approach to elucidating cellular function.

Outcomes

High resolution tomograms of large cellular volumes generated and analyzed in this way have already provided fundamental new insights at a number of levels regarding key structure-function relationships among organelles of the insulin biosynthetic pathway, including the identification of novel connections between compartments within the Golgi complex that are normally spatially/functionally distinct, leading to further debate related to the potential role for direct connections in intra-Golgi transport (28, 39-41, 47, 48). Perhaps the most surprising insight afforded by detailed analysis and segmentation of cellular tomograms has been with regard to the degree of 3D spatial and structural complexity at the subcellular level in the cytoplasm of mammalian cells (32, 49-52) (*Fig. 4*). Indeed, the datasets provided through detailed studies of cellular organization using 3D imaging methods such as ET have attracted considerable attention from within the systems biology and bioinformatics communities due to the significant advantages they would confer by serving as precise (*i.e.* nanometer scale) spatial/structural frameworks for more advanced computational studies aimed at recreating and exploring fundamental cellular processes and biophysical principles *in silico*, from a mathematical/engineering perspective (51, 53, 54).

More recently, to both complement and extend the basic insights derived through high resolution tomography of large cellular volumes (such as those highlighted briefly above), and to move toward a more integrated or 'holistic' approach to understanding the mammalian cell as a prime example of an ordered complex system (52), we have pioneered an approach for imaging and reconstructing mammalian cells (in our case, insulin-secreting beta cells) in their entirety in 3D at intermediate (10-20 nm) resolution. These efforts were driven by the fact that each of our high resolution tomograms constitutes just a narrow cross-sectional 'slab' sliced from a mammalian cell, and typically represents ≤1% of the total cell volume. The 'expedited' approach we have developed yields fully annotated 3D reconstructions of whole cells at ~10 nm resolution within just a few months, partly due to the fact that we have developed new computational tools in parallel that allow us to more efficiently annotate cellular compartments and organelles of interest within the volume (45) (*Fig. 4*). Notably, these new methods have allowed us to quantify subtle changes in mitochondrial structure and organization (number, length, extent of branching/fission/fusion) that reflect the increased energy needs of the beta cell associated with glucose-stimulated insulin biosynthesis and secretory granule exocytosis. We are currently employing this comparative 'whole cell mapping' approach to carry out more detailed investigations aimed at precisely characterizing the nature of the changes that occur at the level of inter-organellar relationships among the key compartments involved in insulin synthesis and release.

Conclusions and future direction

Elucidating the 3D structural organization of molecules, cells and tissues is pivotal to the development of a complete understanding of basic cell and molecular biology, and thus essential to successfully translating that knowledge to improved therapeutic interventions for the prevention and/or treatment of chronic diseases such as diabetes and cancer. High resolution 3D imaging studies of insulin-secreting cells within pancreatic islets have already provided new and unanticipated insights into the complexity of 3D cellular organization that have impacted upon how scientists, students and the public alike picture life at the subcellular level. If current efforts are successful with respect to integrating data related to the 3D structure-function relationships that underpin intra- and inter-cellular interactions, networks and signaling - from molecule-to-cell and from cell-to-tissue – next-generation biologists and clinicians alike will benefit from a more coherent understanding of molecular biology and biochemistry *in situ*.

MOLECULAR TARGETED IMAGING OF ANGIOGENESIS

Angiogenesis represents a complex process of sprouting new capillaries from preexisting vessels and plays an important role in many human diseases such as cancer, coronary artery disease (CAD), diabetes, atherosclerosis, and peripheral artery disease (PAD) (55). The hypoxia-induced angiogenic process initiated by expression of hypoxia-inducible factor 1 (HIF-1α) involves a cascade of events including degradation of the extracellular matrix (ECM) by matrix metalloproteinases (MMPs), proliferation and migration of both smooth muscle and endothelial cells, and the alignment of endothelial cells to form tubes. A number of local and circulating angiogenic factors is involved in this process including vascular endothelial growth factor (VEGF), insulin-like growth factor (IGF-1), angiopoietins, basic fibroblast growth factor (bFGF), and endothelial adhesion molecules – integrins (55, 56).

In a cardiovascular setting the consequence of naturally occurring angiogenesis triggered by hypoxic insult is the restoration of perfusion and oxygenation of ischemic tissues. This process has been traditionally assessed by evaluation of perfusion, function and metabolism (57, 58), however more recently molecular events associated with angiogenesis are studied using novel noninvasive molecular targeted imaging approaches (34, 58-65).

Molecular targeted imaging defined as *in vivo* qualitative or quantitative characterization of biological processes at the cellular, molecular, and whole body level has several requirements; choice of molecular target, choice of probe, and selection of imaging technology. Historically, the earliest targeted imaging approaches utilizing a direct probe-target

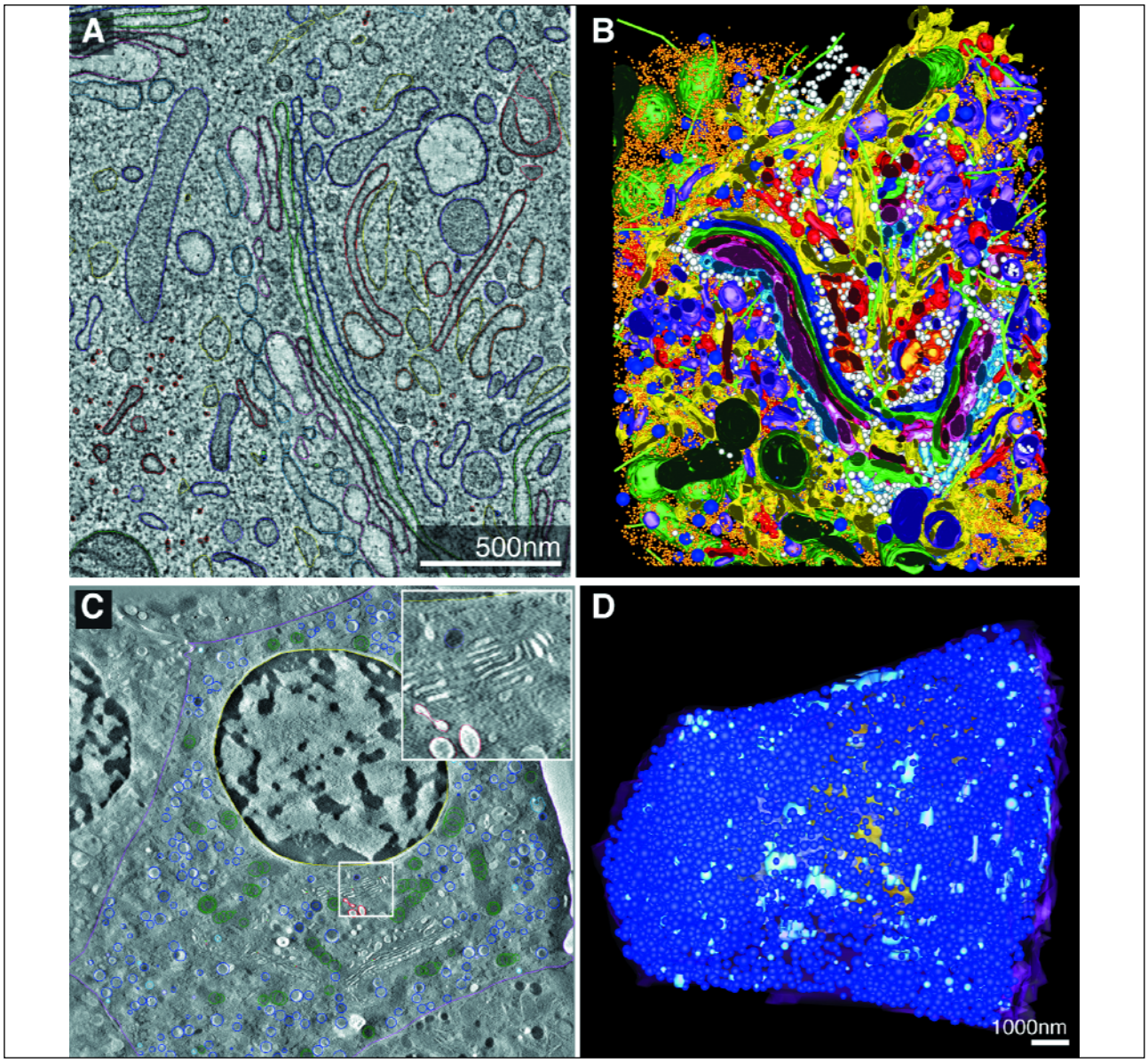

Fig 4. Example of the 3D spatial complexity of cellular organization as visualized by electron microscope tomography. With a view to identifying how and where defects can occur as insulin is trafficked along compartments of the regulated secretory pathway after synthesis in the endoplasmic reticulum (ER), we have developed and employed new imaging and computational approaches for mapping beta cell biology in 3D at high resolution, first for cell culture models for insulin secretion (39) (*A* and *B*), then for beta cells preserved *in situ* in pancreatic islet tissue isolated from mice (41, 45) (*C* and *D*) and humans. (*A*) A magnified view from part of a single pixel-thick image slice extracted from the 315 slices that together comprised the high resolution (~6 nm) 3D reconstruction (3.1 x 3.2 x 1.2 μm^3), which was estimated to represent approximately 1% of that cell's total volume. The center of the region reveals the stacked membranes of the Golgi complex in an insulin-secreting pancreatic beta cell (reproduced from data originally published in: 'Organellar relationships in the Golgi region of the pancreatic beta cell line, HIT-T15, visualized by high resolution electron tomography' (39)). Each individual compartment was 'segmented' by manually tracing along the compartment's bounding membrane across each/every tomographic slice that the object spanned in Z through the volume using the *IMOD* software package (46) in order to precisely define each spatially distinct compartment as a separate object within the tomogram. (*B*) Contours belonging to the same surface were then meshed (in a manner akin to computer graphic animation) such that objects could be (1.) visualized in 3D, and (2.) quantitative data computed for basic morphometric parameters (*e.g.* surface area and volume) using the triangular mesh data for the objects. In the example shown here, the stacked membranes (i.e. 'cisternae') of the Golgi complex are displayed in the context of all other neighboring organelles, vesicles, ribosomes and microtubules in the region. Color-coding: Golgi cisternae (cis-trans): *light blue, pink, cherry, green, dark blue, gold, red*), endoplasmic reticulum (*yellow*), membrane-bound ribosomes (*blue*), free ribosomes (*orange*), microtubules (*bright green*), insulin granules (*blue*), clathrin-negative vesicles (*white*), clathrin-positive compartments and vesicles (*red*), clathrin-negative compartments/vesicles (*purple)* and mitochondria (*dark green*). Scale Bar, 500 nm. (*C*) A digital slice (in the XY plane) extracted from a cellular tomogram of an islet beta cell reconstructed in toto in 3D at ~15 nm resolution. The boxed area (*inset*) reveals the relative clarity of Golgi membranes for comparison with the higher resolution data shown in (*A*). (*D*) The distribution of the 8250 mature (*dark blue*) and 520 immature (*light blue*) insulin granules within the cellular volume that corresponds to the image slice data presented in (*C*) are revealed [reproduced from data originally published in: 'Expedited approaches to whole cell electron tomography and organelle mark-up *in situ* in high-pressure frozen pancreatic islets' (45). Scale Bar, 1000 nm.

interaction concept involved native antibodies, which suffered from high background activity and long clearance times. These undesired characteristics were eliminated by using engineered antibodies and peptide or peptidomimetic probes for imaging of cell-specific antigens. However this direct imaging approach requires a synthesis of a customized probe for every target of interests. To overcome this limitation, indirect imaging approaches were proposed including reporter gene technology, which involves introduction of a reporter gene into cell nuclei and detection of the reporter protein by using radioactive ligands or reporter protein-specific probes. This complex technique was described in detail in previous reviews (34, 65, 66).

The selection of an appropriate molecular target which represents the process to be studied, and the selection of probe which should have high affinity towards the molecular target are critical to the specificity of any imaging approach. On the other hand, imaging technology should provide the best combination of sensitivity and both temporal and spatial resolution.

During recent decades a number of novel imaging modalities and new high-sensitivity and high-resolution imaging systems have been developed, however only a few are available for a broad use in molecular imaging. True multidimensional nuclear techniques such as single photon emission computed tomography (SPECT) and positron emission tomography (PET) using beta-, gamma- or positron-emitting radioisotopes are particularly well suited for *in vivo* molecular imaging due to high sensitivity (picomolar), spatial resolution (submillimeter-to-millimeter), and availability of SPECT, PET scanners and molecular probes. Both modalities present distinct advantages, but also suffer from disadvantages based on the physical and chemical characteristics described in detail elsewhere (67-69), therefore the decision which technique to use should be based on the assessment of the biological system to be studied, availability of radiolabeled molecular probes, and accessibility to the instrumentation.

Recent clinical trials of stimulated angiogenesis in CAD and PAD to induce new blood vessel growth and thereby improve perfusion, tissue oxygenation, substrate exchange, and function, demonstrated no clear benefit over placebo, despite positive results in animal studies (70-76). The evaluation of therapeutic angiogenesis in these trials has focused on a number of clinical endpoints such as exercise tolerance, quality of life, and survival. Therefore there is a need to develop noninvasive approaches for direct evaluation of the molecular events associated with angiogenesis by use of direct biologic markers of the angiogenic process. Potential biologic targets for imaging angiogenesis were identified by the panel of the American Society of Nuclear Cardiology experts during Invitation Meeting in Lake Tahoe in 2002 (77). Among other recommendations, in particular VEGF, VEGF receptors, and integrins have been identified as favorable targets for imaging angiogenesis which put focus on the development of nuclear probes for these specific targets. The potential for targeted imaging of the αvβ3 integrin and VEGF receptors has been demonstrated in animal models of ischemia-induced peripheral and myocardial angiogenesis as outlined below.

$VEGF_{121}$ isoform was used as a targeting ligand for both SPECT and PET studies to assess angiogenic process by imaging VEGF receptor in animal models of both tumor and ischemia-induced peripheral and myocardial angiogenesis (60, 64, 78). Initial studies involved ^{111}Indium labeled $VEGF_{121}$ for SPECT imaging of angiogenesis in a rabbit model of hindlimb ischemia (78). A few years later Cai *et al.* successfully identified angiogenic tumor vasculature in mice using positron-emitting ^{64}Cu-labeled $VEGF_{121}$ (60). More recently the same group developed a PET tracer, ^{64}Cu-6-DOTA-$VEGF_{121}$, which was used to image myocardial angiogenesis in rats at various time points post myocardial infarction induced by the left coronary artery ligation (64). This study demonstrated that ^{64}Cu-6-DOTA-$VEGF_{121}$ preferentially localized in the infarct region with the maximum radiotracer uptake at day 3 post myocardial infarction which was validated by immunohistochemistry of VEGF receptor expression. Other groups developed cardiac-specific reporter as a gene expression system to be used in PET imaging of VEGF receptor in rats (79) and porcine myocardium following adenoviral transfer (80).

The integrins, a family of endothelial cell membrane receptors which serve as adhesion proteins, are involved in a number of cellular processes including angiogenesis. Particularly αvβ3 integrin containing RGD (Arg-Gly-Asp) motif is abundantly expressed on proliferating endothelial cells and is required for angiogenesis-associated cellular processes including endothelial cell migration. Multiple groups of investigators proposed using αvβ3 integrin as a potential target for imaging angiogenesis. The earliest studies were focused on tumor angiogenesis and involved using human monoclonal antibody (LM609) for *in vivo* magnetic resonance imaging of angiogenesis. This approach suffered from slow clearance rate of the antibody, therefore more recently new RGD peptides with high affinity for αvβ3 integrin have been identified and successfully used for imaging angiogenesis (58, 81). The phage-display screening identified the cyclo-(Arg-Gly-Asp-D-Phe-Val) which demonstrated a potent inhibitory activity towards αvβ3 integrin and was used for SPECT and PET imaging of tumor-associated angiogenesis (82-85). Others evaluated an ^{111}In-labeled quinolone (RP748) for noninvasive assessment of myocardial angiogenesis. Meoli *et al.* reported successful application of RP748 for imaging myocardial angiogenesis in rats and dogs after myocardial infarction (86). RP748 uptake localized in the infarct regions and was associated with increased expression and activity of αvβ3 integrin in hypoperfused myocardial segments. More recently, Kalinowski *et al.* demonstrated the relationship between RP748, myocardial perfusion (assessed with ^{99m}Tc-sestamibi) and hypoxia (assessed with ^{99m}Tc-labeled nitroimidazole) in rodent and canine models of myocardial ischemia (87). Other groups evaluated RGD-containing peptide ^{99m}Tc-NC100692 for imaging myocardial and peripheral angiogenesis in animal models of CAD and PAD. Initial reports demonstrated efficacy, safety, metabolic stability and favorable biodistribution of the radiotracer (88-90). Hua *et al.* demonstrated that NC100692 preferentially localized within the ischemic hindlimb after ligation of the right femoral artery in mice. High resolution planar SPECT image analysis was validated with gamma well counting of muscle tissues indicating NC100692 maximal uptake at 1 week after the surgery in consent with increase in capillary density assessed by immunohistochemistry (61). Shortly after this initial report, NC100692 was used to assess myocardial angiogenesis in mice lacking matrix metalloproteinase MMP-9 (62) and in rats subjected to intramyocardial insulin-like growth factor (IGF-1) gene transfer after myocardial infarction (91).

With the availability of dedicated hybrid small animal microSPECT-CT and microPET-CT scanners it become possible not only to localize radiotracer uptake with help of reference CT image (*Fig. 5, 6A*) but also to develop novel approaches to quantify microSPECT or microPET images acquired serially at various time points (*Fig. 6B*) (92). Using irregular regions-of-interests (ROIs) defined on CT reference image to quantify NC100692 uptake within the ischemic hindlimb, Dobrucki *et al.* demonstrated that mice lacking the gene for endothelial nitric oxide synthase (eNOS) have impaired peripheral angiogenesis (92-94). Similar observations were made in diabetic mice subjected to femoral artery occlusion (95).

To complement the strengths of PET (sensitivity) and SPECT (resolution) imaging, few groups put effort at design and development of bifunctional multimeric RGD peptides for SPECT and PET imaging of angiogenesis by incorporating both ^{99m}Tc and ^{64}Cu radioisotope, respectively (96). More recent

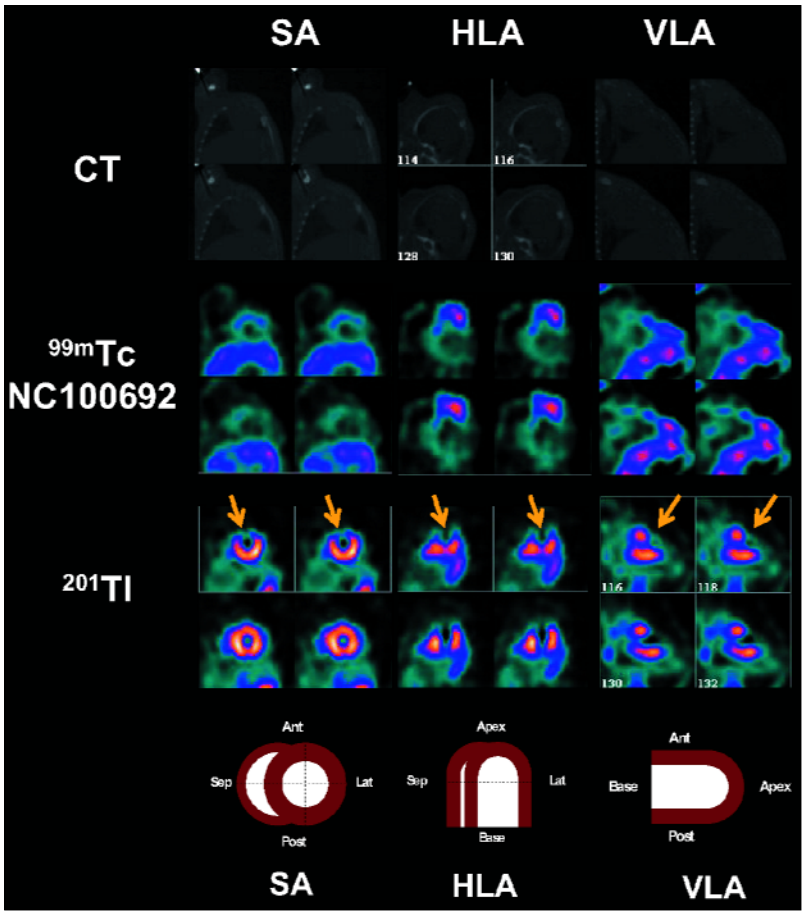

Fig. 5. Representative *in vivo* short axis (SA), vertical long axis (VLA) and horizontal long axis (HLA) X-ray CT, ^{99m}Tc-NC100692 and ^{201}Tl chloride images from C57BL6 mouse at 1 week after myocardial infarction. ^{99m}Tc-NC100692 images were registered with ^{201}Tl chloride perfusion images and X-ray CT images to better demonstrate localization of ^{99m}Tc-NC100692 activity within the heart. Arrows on ^{201}Tl chloride images indicate the regions of perfusion defect (infarct). This corresponds to the regions of increased ^{99m}Tc-NC100692 activity in the anterior wall of infarcted heart. The images were acquired with dedicated small animal hybrid microSPECT-CT scanner (X-FLEX, GE Healthcare).

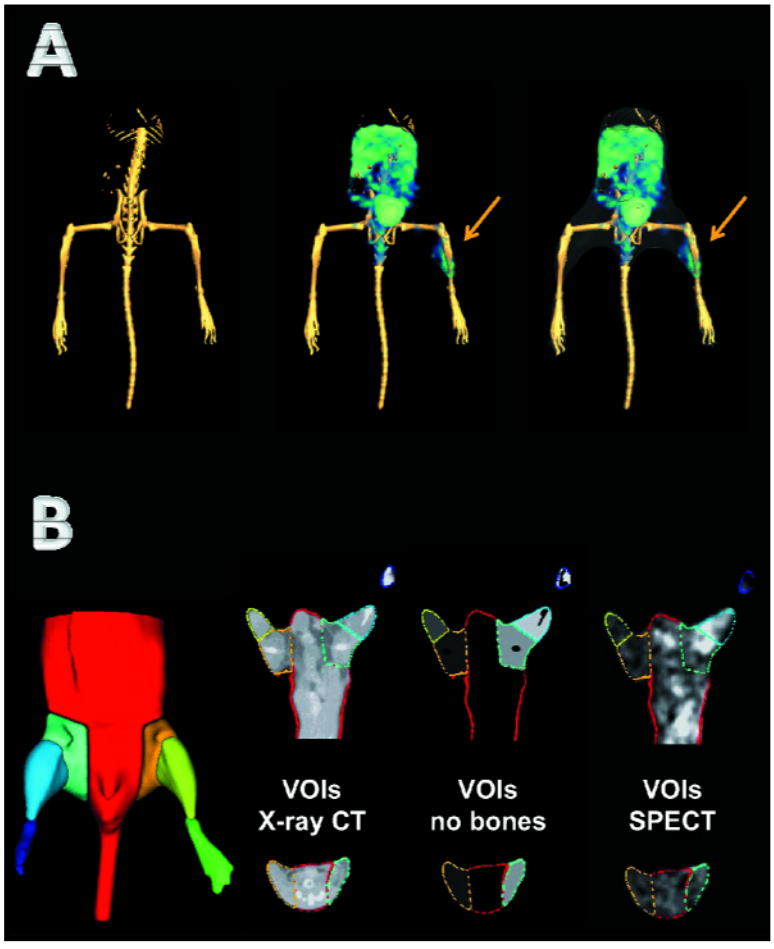

Fig. 6. Representative hybrid microSPECT-CT ^{99m}Tc-NC100692 images of peripheral angiogenesis in murine model of hindlimb ischemia. (*A*) microCT images of bone structures and skin were registered with microSPECT images of ^{99m}Tc-NC100692 targeted at αvβ3 integrin to better demonstrate localization of the radiotracer within ischemic hindlimb marked by yellow arrows. (*B*) microCT images can be also used to quantify radiotracer uptake in soft tissues within ischemic or nonischemic hindlimb. Planes were interactively positioned over lower body of mice to segment microCT image to generate multiple volumes-of-interests (VOIs). Contours of these VOIs are illustrated superimposed on representative microCT image. Segmentation was performed to eliminate bones from VOIs. This complex irregular object map was applied to registered microSPECT images to determine radiotracer activity in each VOI.

developments in imaging strategies to assess angiogenesis involved using ^{76}Br-labeled biodegradable nanoparticles targeted at $\alpha v\beta 3$ integrin (59). These constructs contain polyethylene oxide (PEO) chains which allow tuning biodistribution and clearance rate of the parent targeted nanoparticles by modifying length and branching of the PEO chains.

All above studies indicate that radiolabeled agents targeted at molecular markers of the angiogenic process can be a valuable tool to assess both naturally occurring and therapeutic angiogenesis. Development of new hybrid scanners combining anatomical (CT, MRi) and functional (SPECT, PET) imaging modalities, design of novel targeted probes and reporter gene systems, as well as availability of interdisciplinary teams consisting of biologists, chemists, physiologists, physicians and engineers will result in a tremendous growth in the field of molecular targeted imaging. All this will allow better understanding of fundamental biologic processes and noninvasive monitoring of therapeutic interventions in living systems with a great potential to translate to clinical practice.

Acknowledgements: Research related to the work discussed here has been supported by grants from the Ministry of Science and Higher Education in Poland (2/PO5F/029/29, PBZ-KBN-101/T09/2003/10, 0471/B/P01/2009/37), as well as the Juvenile Diabetes Research Foundation International (2-2004-275, 25-2007-848 and 10-2006-726) and National Institutes of Health (DK-71236) in the USA. BJM is a Chief Investigator of the Australian Research Council (ARC) Centre of Excellence in Bioinformatics (CE0561992). The Advanced Cryo-Electron Microscopy Laboratory housed at the Institute for Molecular Bioscience is a major node of the Australian Microscopy and Microanalysis Research Facility (AMMRF).

All authors contributed to the manuscript equally.

Conflict of interests: None declared.

REFERENCES

1. Kalinowski L, Malinski T. Endothelial NADH/NADPH-dependent enzymatic sources of superoxide production: relationship to endothelial dysfunction. *Acta Biochim Pol* 2004; 51: 459-469.
2. Landmesser U, Hornig B, Drexler H. Endothelial function: a critical determinant in atherosclerosis? *Circulation* 2004;109: II27-II33.
3. Heitzer T, Schlinzig T, Krohn K, Meinertz T, Munzel T. Endothelial dysfunction, oxidative stress, and risk of cardiovascular events in patients with coronary artery disease. *Circulation* 2001; 104: 2673-2678.
4. Channon KM, Guzik TJ. Mechanisms of superoxide production in human blood vessels: relationship to endothelial dysfunction, clinical and genetic risk factors. J *Physiol Pharmacol* 2002; 53: 515-524.
5. Huang PL, Huang Z, Mashimo H, *et al.* Hypertension in mice lacking the gene for endothelial nitric oxide synthase. *Nature* 1995; 377: 239-242.
6. Ohashi Y, Kawashima S, Hirata K, *et al.* Hypotension and reduced nitric oxide-elicited vasorelaxation in transgenic mice overexpressing endothelial nitric oxide synthase. *J Clin Invest* 1998; 102: 2061-2071.
7. Forstermann U, Munzel T. Endothelial nitric oxide synthase in vascular disease: from marvel to menace. *Circulation* 2006; 113: 1708-1714.
8. Fulton D, Gratton JP, Sessa WC. Post-translational control of endothelial nitric oxide synthase: why isn't calcium/calmodulin enough? *J Pharmacol Exp Ther* 2001; 299: 818-824.
9. McCabe TJ, Fulton D, Roman LJ, Sessa WC. Enhanced electron flux and reduced calmodulin dissociation may explain "calcium-independent" eNOS activation by phosphorylation. *J Biol Chem* 2000; 275: 6123-6128.
10. Lin MI, Fulton D, Babbitt R, *et al.* Phosphorylation of threonine 497 in endothelial nitric-oxide synthase coordinates the coupling of L-arginine metabolism to efficient nitric oxide production. *J Biol Chem* 2003; 278: 44719-44726.
11. Michell BJ, Harris MB, Chen ZP, *et al.* Identification of regulatory sites of phosphorylation of the bovine endothelial nitric-oxide synthase at serine 617 and serine 635. *J Biol Chem* 2002; 277: 42344-42351.
12. Chen CA, Druhan LJ, Varadharaj S, Chen YR, Zweier JL. Phosphorylation of endothelial nitric-oxide synthase regulates superoxide generation from the enzyme. *J Biol Chem* 2008; 283: 27038-27047.
13. Pacher P, Beckman JS, Liaudet L. Nitric oxide and peroxynitrite in health and disease. *Physiol Rev* 2007; 87: 315-424.
14. Zou MH, Shi C, Cohen RA. Oxidation of the zinc-thiolate complex and uncoupling of endothelial nitric oxide synthase by peroxynitrite. *J Clin Invest* 2002; 109: 817-826.
15. Laursen JB, Somers M, Kurz S, *et al.* Endothelial regulation of vasomotion in apoE-deficient mice: implications for interactions between peroxynitrite and tetrahydrobiopterin. *Circulation* 2001; 103: 1282-1288.
16. Bendall JK, Alp NJ, Warrick N, *et al.* Stoichiometric relationships between endothelial tetrahydrobiopterin, endothelial NO synthase (eNOS) activity, and eNOS coupling in vivo: insights from transgenic mice with endothelial-targeted GTP cyclohydrolase 1 and eNOS overexpression. *Circ Res* 2005; 97: 864-871.
17. Landmesser U, Dikalov S, Price SR, *et al.* Oxidation of tetrahydrobiopterin leads to uncoupling of endothelial cell nitric oxide synthase in hypertension. *J Clin Invest* 2003; 111: 1201-1209.
18. Milstien S, Katusic Z. Oxidation of tetrahydrobiopterin by peroxynitrite: implications for vascular endothelial function. *Biochem Biophys Res Commun* 1999; 263: 681-684.
19. Kalinowski L, Dobrucki IT, Malinski T. Race-specific differences in endothelial function: predisposition of African Americans to vascular diseases. *Circulation* 2004; 109: 2511-2517.
20. Brovkovych VV, Kalinowski L, Muller-Peddinghaus R, Malinski T. Synergistic antihypertensive effects of nifedipine on endothelium: concurrent release of NO and scavenging of superoxide. *Hypertension* 2001; 37: 34-39.
21. Kalinowski L, Dobrucki IT, Malinski T. Cicletanine stimulates nitric oxide release and scavenges superoxide in endothelial cells. *J Cardiovasc Pharmacol* 2001; 37: 713-724.
22. Kalinowski L, Dobrucki IT, Malinski T. Cerivastatin potentiates nitric oxide release and enos expression through inhibition of isoprenoids synthesis. *J Physiol Pharmacol* 2002; 53: 585-595.
23. Kalinowski L, Dobrucki LW, Brovkovych V, Malinski T. Increased nitric oxide bioavailability in endothelial cells contributes to the pleiotropic effect of cerivastatin. *Circulation* 2002; 105: 933-938.
24. Kalinowski L, Dobrucki LW, Szczepanska-Konkel M, *et al.* Third-generation beta-blockers stimulate nitric oxide release from endothelial cells through ATP efflux: a novel mechanism for antihypertensive action. *Circulation* 2003; 107: 2747-2752.
25. Kalinowski L, Matys T, Chabielska E, Buczko W, Malinski T. Angiotensin II AT1 receptor antagonists inhibit platelet adhesion and aggregation by nitric oxide release. *Hypertension* 2002; 40: 521-527.
26. Mason RP, Kalinowski L, Jacob RF, Jacoby AM, Malinski T. Nebivolol reduces nitroxidative stress and restores nitric

oxide bioavailability in endothelium of black Americans. *Circulation* 2005; 112: 3795-3801.
27. Porter KR. A study of tissue culture cells by electron microscopy: methods and preliminary observations. *J Exp Med* 1945; 81: 233-246.
28. Marsh BJ. Lessons from tomographic studies of the mammalian Golgi. *Biochim Biophys Acta* 2005; 1744: 273-292.
29. Marsh BJ. Reconstructing mammalian membrane architecture by large area cellular tomography. *Methods Cell Biol* 2007; 79: 193-220.
30. Mastronarde DN. Dual-axis tomography: an approach with alignment methods that preserve resolution. *J Struct Biol* 1997; 120: 343-352.
31. McEwen BF, Marko M. The emergence of electron tomography as an important tool for investigating cellular ultrastructure. *J Histochem Cytochem* 2001; 49: 553-564.
32. McIntosh R, Nicastro D, Mastronarde D. New views of cells in 3D: an introduction to electron tomography. *Trends Cell Biol* 2005; 15: 43-51.
33. Perkins GA, Renken CW, Song JY, *et al.* Electron tomography of large, multicomponent biological structures. *J Struct Biol* 1997; 120: 219-227.
34. Dobrucki LW, Sinusas AJ. Imaging angiogenesis. *Curr Opin Biotechnol* 2007; 18: 90-96.
35. Kennedy JA, Israel O, Frenkel A, Bar-Shalom R, Azhari H. Super-resolution in PET imaging. *IEEE Trans Med Imaging* 2006; 25: 137-147.
36. Kubota T, Yamada K, Ito H, Kizu O, Nishimura T. High-resolution imaging of the spine using multidetector-row computed tomography: differentiation between benign and malignant vertebral compression fractures. *J Comput Assist Tomogr* 2005; 29: 712-719.
37. Pouwels PJ, Kuijer JP, Mugler JP 3rd, Guttmann CR, Barkhof F. Human gray matter: feasibility of single-slab 3D double inversion-recovery high-spatial-resolution MR imaging. *Radiology* 2006; 241: 873-879.
38. Ladinsky MS, Mastronarde DN, McIntosh JR, Howell KE, Staehelin LA. Golgi structure in three dimensions: functional insights from the normal rat kidney cell. *J Cell Biol* 1999; 144: 1135-1149.
39. Marsh BJ, Mastronarde DN, Buttle KF, Howell KE, McIntosh JR. Organellar relationships in the Golgi region of the pancreatic beta cell line, HIT-T15, visualized by high resolution electron tomography. *Proc Natl Acad Sci USA* 2001; 98: 2399-2406.
40. Marsh BJ, Mastronarde DN, McIntosh JR, Howell KE. Structural evidence for multiple transport mechanisms through the Golgi in the pancreatic beta-cell line, HIT-T15. *Biochem Soc Trans* 2001; 29: 461-467.
41. Marsh BJ, Volkmann N, McIntosh JR, Howell KE. Direct continuities between cisternae at different levels of the Golgi complex in glucose-stimulated mouse islet beta cells. *Proc Natl Acad Sci USA* 2004; 101: 5565-5570.
42. Sosinsky GE, Crum J, Jones YZ, *et al.* The combination of chemical fixation procedures with high pressure freezing and freeze substitution preserves highly labile tissue ultrastructure for electron tomography applications. *J Struct Biol* 2008; 161: 359-371.
43. Dudek RW, Boyne AF. An excursion through the ultrastructural world of quick-frozen pancreatic islets. *Am J Anat* 1986; 175: 217-243, 354.
44. Gilkey JC, Staehelin LA. Advances in ultrarapid freezing for the preservation of cellular ultrastructure. *J Electron Microsc Tech* 1986; 3: 177-210.
45. Noske AB, Costin AJ, Morgan GP, Marsh BJ. Expedited approaches to whole cell electron tomography and organelle mark-up in situ in high-pressure frozen pancreatic islets. *J Struct Biol* 2008; 161: 298-313.
46. Kremer JR, Mastronarde DN, McIntosh JR. Computer visualization of three-dimensional image data using IMOD. *J Struct Biol* 1996; 116: 71-76.
47. Marsh BJ, Howell KE. The mammalian Golgi-complex debates. *Nat Rev Mol Cell Biol* 2002; 3: 789-795.
48. Mogelsvang S, Marsh BJ, Ladinsky MS, Howell KE. Predicting function from structure: 3D structure studies of the mammalian Golgi complex. *Traffic* 2004; 5: 338-345.
49. Baumeister W. Electron tomography: towards visualizing the molecular organization of the cytoplasm. *Curr Opin Struct Biol* 2002; 12: 679-684.
50. Goodsell DS. Making the step from chemistry to biology and back. *Nat Chem Biol* 2007; 3: 681-684.
51. Lehner B, Tischler J, Fraser AG. Systems biology: where it's at in 2005. *Genome Biol* 2005; 6: 338.
52. Rafelski SM, Marshall WF. Building the cell: design principles of cellular architecture. *Nat Rev Mol Cell Biol* 2008; 9: 593-602.
53. Bork P, Serrano L. Towards cellular systems in 4D. *Cell* 2005; 121: 507-509.
54. Burrage K, Hood L, Ragan MA. Advanced computing for systems biology. *Brief Bioinform* 2006; 7: 390-398.
55. Battegay EJ. Angiogenesis: mechanistic insights, neovascular diseases, and therapeutic prospects. *J Mol Med* 1995; 73: 333-346.
56. Carmeliet P. Angiogenesis in health and disease. *Nat Med* 2003; 9: 653-660.
57. Yang HT, Prior BM, Lloyd PG, *et al.* Training-induced vascular adaptations to ischemic muscle. *J Physiol Pharmacol* 2008; 59(Suppl 7): 57-70.
58. Sinusas AJ. Imaging of angiogenesis. *J Nucl Cardiol* 2004; 11: 617-633.
59. Almutairi A, Rossin R, Shokeen M, *et al.* Biodegradable dendritic positron-emitting nanoprobes for the noninvasive imaging of angiogenesis. *Proc Natl Acad Sci USA* 2009; 106: 685-690.
60. Cai W, Chen K, Mohamedali KA, *et al.* PET of vascular endothelial growth factor receptor expression. *J Nucl Med* 2006; 47: 2048-2056.
61. Hua J, Dobrucki LW, Sadeghi MM, *et al.* Noninvasive imaging of angiogenesis with a 99mTc-labeled peptide targeted at alphavbeta3 integrin after murine hindlimb ischemia. *Circulation* 2005; 111: 3255-3260.
62. Lindsey ML, Escobar GP, Dobrucki LW, *et al.* Matrix metalloproteinase-9 gene deletion facilitates angiogenesis after myocardial infarction. *Am J Physiol Heart Circ Physiol* 2006; 290: H232-H239.
63. Morrison MS, Ricketts SA, Barnett J, Cuthbertson A, Tessier J, Wedge SR. Use of a novel Arg-Gly-Asp radioligand, 18F-AH111585, to determine changes in tumor vascularity after antitumor therapy. *J Nucl Med* 2009; 50: 116-122.
64. Rodriguez-Porcel M, Cai W, Gheysens O, *et al.* Imaging of VEGF receptor in a rat myocardial infarction model using PET. *J Nucl Med* 2008; 49: 667-673.
65. Sinusas AJ, Bengel F, Nahrendorf M, *et al.* Multimodality cardiovascular molecular imaging, part I. *Circ Cardiovasc Imaging* 2008; 1: 244-256.
66. Inubushi M, Tamaki N. Radionuclide reporter gene imaging for cardiac gene therapy. *Eur J Nucl Med Mol Imaging* 2007; 34(Suppl 1): S27-S33.
67. Dobrucki LW, Sinusas AJ. Molecular imaging. A new approach to nuclear cardiology. *Q J Nucl Med Mol Imaging* 2005; 49: 106-115.
68. Dobrucki LW, Sinusas AJ. Molecular cardiovascular imaging. *Curr Cardiol Rep* 2005; 7: 130-135.

69. Dobrucki LW, Sinusas AJ. Cardiovascular molecular imaging. *Semin Nucl Med* 2005; 35: 73-81.
70. Grines CL, Watkins MW, Helmer G, *et al.* Angiogenic Gene Therapy (AGENT) trial in patients with stable angina pectoris. *Circulation* 2002; 105: 1291-1297.
71. Hedman M, Hartikainen J, Syvanne M, *et al.* Safety and feasibility of catheter-based local intracoronary vascular endothelial growth factor gene transfer in the prevention of postangioplasty and in-stent restenosis and in the treatment of chronic myocardial ischemia: phase II results of the Kuopio Angiogenesis Trial (KAT). *Circulation* 2003; 107: 2677-2683.
72. Henry TD, Annex BH, McKendall GR, *et al.* The VIVA trial: Vascular endothelial growth factor in ischemia for vascular angiogenesis. *Circulation* 2003; 107: 1359-1365.
73. Kleiman NS, Califf RM. Results from late-breaking clinical trials sessions at ACCIS 2000 and ACC 2000. *J Am Coll Cardiol* 2000; 36: 310-325.
74. Lederman RJ, Mendelsohn FO, Anderson RD, *et al.* Therapeutic angiogenesis with recombinant fibroblast growth factor-2 for intermittent claudication (the TRAFFIC study): a randomised trial. *Lancet* 2002; 359: 2053-2058.
75. Rajagopalan S, Mohler ER 3rd, Lederman RJ, *et al.* Regional angiogenesis with vascular endothelial growth factor in peripheral arterial disease: a phase II randomized, double-blind, controlled study of adenoviral delivery of vascular endothelial growth factor 121 in patients with disabling intermittent claudication. *Circulation* 2003; 108: 1933-1938.
76. Simons M, Bonow RO, Chronos NA, *et al.* Clinical trials in coronary angiogenesis: issues, problems, consensus: An expert panel summary. *Circulation* 2000; 102: E73-E86.
77. Lake Tahoe invitation meeting 2002. *J Nucl Cardiol* 2003; 10: 223-257.
78. Lu E, Wagner WR, Schellenberger U, *et al.* Targeted in vivo labeling of receptors for vascular endothelial growth factor: approach to identification of ischemic tissue. *Circulation* 2003; 108: 97-103.
79. Wu JC, Inubushi M, Sundaresan G, Schelbert HR, Gambhir SS. Positron emission tomography imaging of cardiac reporter gene expression in living rats. *Circulation* 2002; 106: 180-183.
80. Wagner B, Anton M, Nekolla SG, *et al.* Noninvasive characterization of myocardial molecular interventions by integrated positron emission tomography and computed tomography. *J Am Coll Cardiol* 2006; 48: 2107-2115.
81. Dijkgraaf I, Beer AJ, Wester HJ. Application of RGD-containing peptides as imaging probes for alphavbeta3 expression. *Front Biosci* 2009; 14: 887-899.
82. Haubner R, Weber WA, Beer AJ, *et al.* Noninvasive visualization of the activated alphavbeta3 integrin in cancer patients by positron emission tomography and [18F]Galacto-RGD. *PLoS Med* 2005; 2: e70.
83. Haubner R, Wester HJ, Burkhart F, *et al.* Glycosylated RGD-containing peptides: tracer for tumor targeting and angiogenesis imaging with improved biokinetics. *J Nucl Med* 2001; 42: 326-336.
84. Haubner R, Wester HJ, Reuning U, *et al.* Radiolabeled alpha(v)beta3 integrin antagonists: a new class of tracers for tumor targeting. *J Nucl Med* 1999; 40: 1061-1071.
85. Haubner R, Wester HJ, Weber WA, *et al.* Noninvasive imaging of alpha(v)beta3 integrin expression using 18F-labeled RGD-containing glycopeptide and positron emission tomography. *Cancer Res* 2001; 61: 1781-1785.
86. Meoli DF, Sadeghi MM, Krassilnikova S, *et al.* Noninvasive imaging of myocardial angiogenesis following experimental myocardial infarction. *J Clin Invest* 2004; 113: 1684-1691.
87. Kalinowski L, Dobrucki LW, Meoli DF, *et al.* Targeted imaging of hypoxia-induced integrin activation in myocardium early after infarction. *J Appl Physiol* 2008; 104: 1504-1512.
88. Bach-Gansmo T, Danielsson R, Saracco A, *et al.* Integrin receptor imaging of breast cancer: a proof-of-concept study to evaluate 99mTc-NC100692. *J Nucl Med* 2006; 47: 1434-1439.
89. Edwards D, Jones P, Haramis H, *et al.* 99mTc-NC100692—a tracer for imaging vitronectin receptors associated with angiogenesis: a preclinical investigation. *Nucl Med Biol* 2008; 35: 365-375.
90. Indrevoll B, Kindberg GM, Solbakken M, *et al.* NC-100717: a versatile RGD peptide scaffold for angiogenesis imaging. *Bioorg Med Chem Lett* 2006; 16: 6190-6193.
91. Dobrucki LW, Tsutsumi Y, Kalinowski L, *et al.* Local IGF-1 gene delivery post myocardial infarction affects temporal and regional alpha-v integrin activation as assessed with radiolabelled RGD peptide. *J Nucl Cardiol* 2007; 14: 8.16, S61.
92. Dobrucki LW, Dione DP, Kalinowski L, *et al.* Serial noninvasive targeted imaging of peripheral angiogenesis: validation and application of a semiautomated quantitative approach. *J Nucl Med* 2009; 50: 1356-1363.
93. Dobrucki LW, Dione DP, Kalinowski L, Dione D, Papademetris X, Sinusas AJ. Hybrid microSPECT-CT facilitates quantitative analysis of radiotracer-based images of peripheral angiogenesis. *J Nucl Med* 2007; 48(Suppl 2): 166P.
94. Dobrucki LW, Dione DP, Papademetris X, *et al.* Hybrid microSPECT/CT imaging permits serial quantitative non-invasive evaluation of angiogenesis and arteriogenesis in murine model of hindlimb ischemia. *Mol Imag Biol* 2006; 8: 62.
95. Dobrucki LW, Kalinowski L, Dione DP, *et al.* Targeted imaging of peripheral angiogenesis in type-1 diabetes demonstrates impairment of alpha-v integrin activation associated with glycation. *Diabetes* 2007; 56: A196.
96. Liu S. Radiolabeled multimeric cyclic RGD peptides as integrin alphavbeta3 targeted radiotracers for tumor imaging. *Mol Pharm* 2006; 3: 472-487.

Received: August 5, 2009
Accepted: September 10, 2009

Authors' addresses: Lawrence W. Dobrucki, PhD, Section of Cardiovascular Medicine, Department of Internal Medicine, Yale University School of Medicine, P.O. Box 208017, New Haven, CT 06513, USA; Phone: +1-203-785-4909; Fax: +1-203-785-4007; e-mail: wawrzyniec.dobrucki@yale.edu;

Brad J. Marsh, PhD, Institute for Molecular Bioscience, Centre for Microscopy and Microanalysis, ARC Centre of Excellence in Bioinformatics and School of Chemistry and Molecular Biosciences, The University of Queensland, St Lucia, QLD 4072, Australia; Phone: +61-7-3346-2018; Fax +61-7-3346-2101; e-mail: b.marsh1@uq.edu.au and lekal@gumed.edu.pl

Leszek Kalinowski, MD PhD, Department of Medical Laboratory Diagnostics, Chair of Clinical Chemistry and Biochemistry, Medical University of Gdansk, Debinki 7, 80-211 Gdansk, Poland; Phone: +48-58-349-2791; Fax +48-58-349-2784; E-mail: lekal@amg.gda.pl.